Investigation of deformation behavior of Zr-Ti-Ni-Cu-Be bulk metallic glass containing nanocrystals

G. WANG
School of Materials Science and Engineering,Harbin Institute of Technology, Harbin, 150001, China; Department of Engineering,The Australian National University, Canberra, ACT 0200, Australia

J. SHEN*
School of Materials Science and Engineering,Harbin Institute of Technology, Harbin, 150001, China
E-mail: junshen@public.hr.hl.cn

Q. H. QIN
Department of Engineering,The Australian National University, Canberra, ACT 0200, Australia

J. F. SUN
School of Materials Science and Engineering,Harbin Institute of Technology, Harbin, 150001, China

Z. H. STACHURSKI
Department of Engineering,The Australian National University, Canberra, ACT 0200, Australia

B. D. ZHOU
School of Materials Science and Engineering,Harbin Institute of Technology, Harbin, 150001, China

$Zr_{41.25}Ti_{13.75}Ni_{10}Cu_{12.5}Be_{22.5}$ (at.%) bulk metallic glass (BMG) is annealed at 676 K for various times. The influence of the microstructural evolution on the mechanical properties is studied by tensile test and micro hardness test at room temperature. The structural relaxation due to the short time annealing does not affect the deformation behavior of the BMG. The nanocrystallization inducing embrittlement is due to the presence of nano-scale particles promoting the crack forming and propagating during the tensile deformation. The existence of nano-scale particles also enhances the viscosity of the amorphous phase within the shear band and even obstructs the formation of the shear band at the indenter tip, which results in a strengthening phenomenon in the annealed BMG under the indentation load.

1. Introduction

Recently, bulk metallic glasses, as a kind of material containing no defects controlling the mechanical behavior in their crystalline counterparts, have been extensively investigated. Further, BMGs usually exhibit a appreciable supercooled liquid region ΔT, defined as the temperature interval between the glass transition temperature T_g and the onset crystallization temperature T_x. Due to a drastic drop in viscosity (usually by several orders of magnitude) during the glass transition process upon reheating, it is possible to fabricate near net-shape structural components in this temperature region [1–4]. However, structural evolution of amorphous phase is unavoidable when BMGs are processed in the supercooled liquid region [5–8]. So it is of importance to understand effects of structural evolution on mechanical properties of the BMGs exposed in the supercooled liquid region. The influence of structural evolution resulted from annealing treatment on mechanical properties of BMGs has been widely studied. There were two viewpoints on the effects of annealing treatment on BMGs' mechanical properties. One was that the formation of nanocrystals in annealing treatment would enhance the strength of the BMGs [9–12]. The direct

---

*Author to whom all correspondence should be addressed.

0022-2461
DOI: 10.1007/s10853-005-3081-6

evidences were increase both in fracture strength and in hardness. On the other hand, some studies found that the precipitation of nanocrystalline phase resulted in embrittlement of BMGs and deteriorated mechanical properties, such as impact toughness, fracture strength and strain for annealed BMGs [13–16]. In this paper, we investigate the deformation behavior of annealed $Zr_{41.25}Ti_{13.75}Ni_{10}Cu_{12.5}Be_{22.5}$ BMG subjected to tensile test and microindentation at room temperature.

2. Experimental process

Alloy ingots with nominal composition of $Zr_{41.25}Ti_{13.75}Ni_{10}Cu_{12.5}Be_{22.5}$ were prepared by arc melting a mixture of pure metal elements in a titanium-gettered argon atmosphere, followed by suction casting into copper moulds to form BMG sheet-like samples with a size of 3 × 70 × 30 mm. The annealing treatment was carried out in a quartz tube sealed under vacuum of 10^{-3} Pa. The annealing temperature was controlled to be better than ±1.5 K. The thermal analyses were performed with a TA Instruments 2920 modulated differential scanning calorimeter (DSC). The annealing sequences and crystallization products were examined by transmission electron microscopy (TEM). TEM specimens were prepared by dispersing finely ground the BMG powders onto a holey carbon film supported by microgrid. TEM observations were conducted on a Philips EM430 operating at 300 kV. The X-ray diffraction (XRD) measurements were carried out on a Philips D5000 machine. Tensile deformation tests were conducted using Instron 4505 type machine. Tensile specimens having a gauge length of 11 mm, a thickness of 3 mm and a width of 1.1 mm were fabricated from the plate BMG samples by means of electrical discharge machining. The micro hardness measurement was tested in a MATSUZAWA SEIKI MHT-1 type micro hardness tester. Fracture surface morphology and indent observations were carried out using a Cambridge STEREOSCAN 360 scanning electron microscope (SEM).

3. Results

3.1. DSC, TEM and XRD analysis

The $Zr_{41.25}Ti_{13.75}Ni_{10}Cu_{12.5}Be_{22.5}$ BMG has an excellent glass forming ability and a high thermal stability [17]. However, once the BMG is annealed in the supercooled liquid region, the structural evolution of the amorphous phase will be activated. Fig. 1 shows the DSC traces of as-quenched and pre-annealed BMGs at a heating rate of 20 K/min. The characteristic temperatures for the as-quenched BMG, i.e. T_g and T_x, are respectively 616 and 698 K. Accordingly, the supercooled liquid region, $\Delta T_x = T_x - T_g$, is 82 K. The isothermal annealing temperature was selected to be 676 K, located in the middle of the supercooled liquid region.

For the as-quenched BMG, three crystallization exothermic peaks reflecting a multi-stage crystallization behaviour is observed as shown in Fig. 1a. As the BMG is annealed for 180 s, all exothermic peaks, i.e. T_{p1}, T_{p2} and T_{p3}, shift slightly towards a lower temperature (Fig. 1b). Furthermore, measurement of the crystallization heat, i.e. the area enclosed by the exothermic peaks and the baseline of the DSC curve, shows that the crystallization heat does not change as compared to that of the as-quenched BMG. So the annealing for 180 s results in a slight reduction in thermal stability of the BMG without any indication of crystallization during the annealing. As to the BMG annealed for 360 s, the DSC trace (Fig. 1c) shows that the first exothermic peak is nearly invisible, indicating the occurrence of primary crystallization [18]. For the BMG further annealed for 600 s, the second exothermic peak is smaller, apart from the absence of the first exothermic peak (Fig. 1d), compared to the DSC trace of the as-quenched BMG, demonstrating that the second stage crystallization occurred, following the primary crystallization during annealing. The second stage crystallization evolved more significantly as the BMG was annealed for a longer time, e.g. 1200 s, as shown in Fig. 1e.

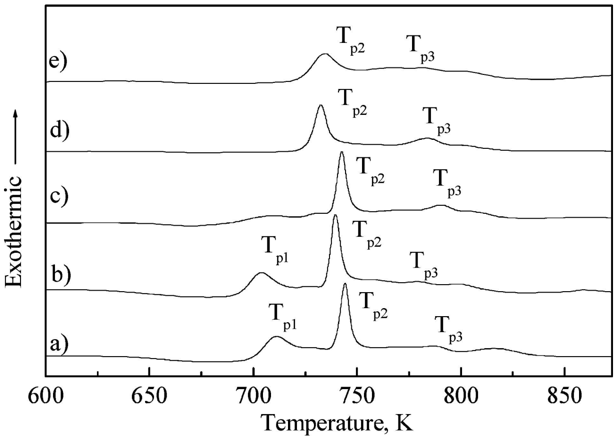

Figure 1 DSC curves of the as-cast sample (a) and the samples annealed at 676 K for 180 s (b), 360 s (c), 600 s (d) and 1200 s (e).

To further clarify the structural evolution of the BMG annealed for 180 s, the specific heat, c_p, of the as-quenched sample and the sample annealed for 180 s were calculated from DSC traces shown in Fig. 2, the value of c_p for the as-quenched BMG exhibits a signifi-

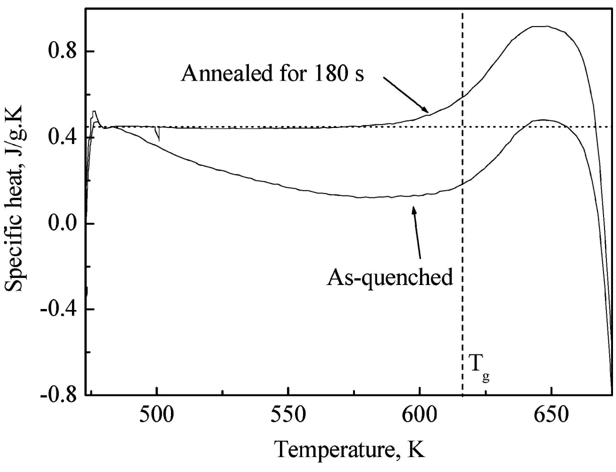

Figure 2 Specific heats of the as-quenched and annealed (for 180 s) BMGs, deduced from their DSC traces.

TABLE I Crystallized volume fraction (V_c), tensile fracture strength (σ_f), Young's modulus (E) and micro hardness (Hv) of the BMG annealed at 676 K for various times

	Annealing time (s)				
	0	180	360	600	1200
V_c (%)	–	0	13	29	53
σ_f (MPa)	1848	1846	1675	1276	669
E (GPa)	88.6	89.6	94.4	97.7	102.6
Hv	522	527	540	588	657

cant decrease before glass transition temperature, T_g, as compared to that of the annealed BMG. The decrease in the value of c_p for the as-quenched BMG results from a structural relaxation during continuous heating. And the structural relaxation would induce the reduction in the quantity of the free volume [19, 20]. The annihilation of the free volume, as a kind of defects, will promote the degree of order of the amorphous phase and bring out some ordered domains. On reheating, these ordered domains will become the potential nucleation sites for crystallization. In comparison, the specific heat of the 180 s annealed sample does not change much during the continuous DSC testing under glass transition temperature, suggesting that the material has suffered structural relaxation upon annealing. Therefore, the thermal stability of the BMG decreases after annealing for 180 s as evidenced by the slight shift of the peak crystallization temperatures respect to those of the as-quenched sample. In addition, the annihilation of the free volume can densify the amorphous material, which should affect the mechanical properties [13].

Based on the DSC traces in Fig. 1, the crystallization heat can be measured by integrating the area of exothermic peak. The crystallized volume fraction is roughly calculated by an equation [21]: $V_c = (\Delta H_f - \Delta H_a)/\Delta H_f$, where ΔH_f is the crystallization heat of the as-quenched BMG, ΔH_a is the crystallization heat of the annealed BMG. The crystallized volume fractions corresponding specimens annealed for different times are tabulated in Table I.

Fig. 3 presents the TEM micrographs of the annealed BMG. As can be seen that annealing for 360 s results in precipitation of nanocrystals with a size of approximately 5 nm crystallizing from amorphous matrix (see Fig. 3a). The corresponding dark field image, taken with the objective aperture centred on the inner ring of selected area electron diffraction (SAED) pattern, shows nanocrystals homogeneously distributing on the amorphous matrix (see Fig. 3b). However, the SAED pattern shows one strong inner ring plus one faint outer ring, which is very similar to those of the as-quenched BMG [22]. This is because the nanocrystalline phase is small in size (~5 nm) and in volume fraction (~13%). For the BMG annealed for 600 s, both the HRTEM image and the dark field image clearly show the presence of nanocrystals with the size of about 15 nm embedding on the amorphous matrix (see Figs 3c and d). The corresponding SAED pattern shows a strong inner ring with a weak ring located at the higher diffraction angle being overlapped by many diffraction spots, indicating the presence of a substantial amount of the amorphous phase. This is in accordance with the crystallized volume fraction of 29% measured from the DSC trace (Table I). Nanocrystals coarsened upon increasing the duration of annealing up to 1200 s (see

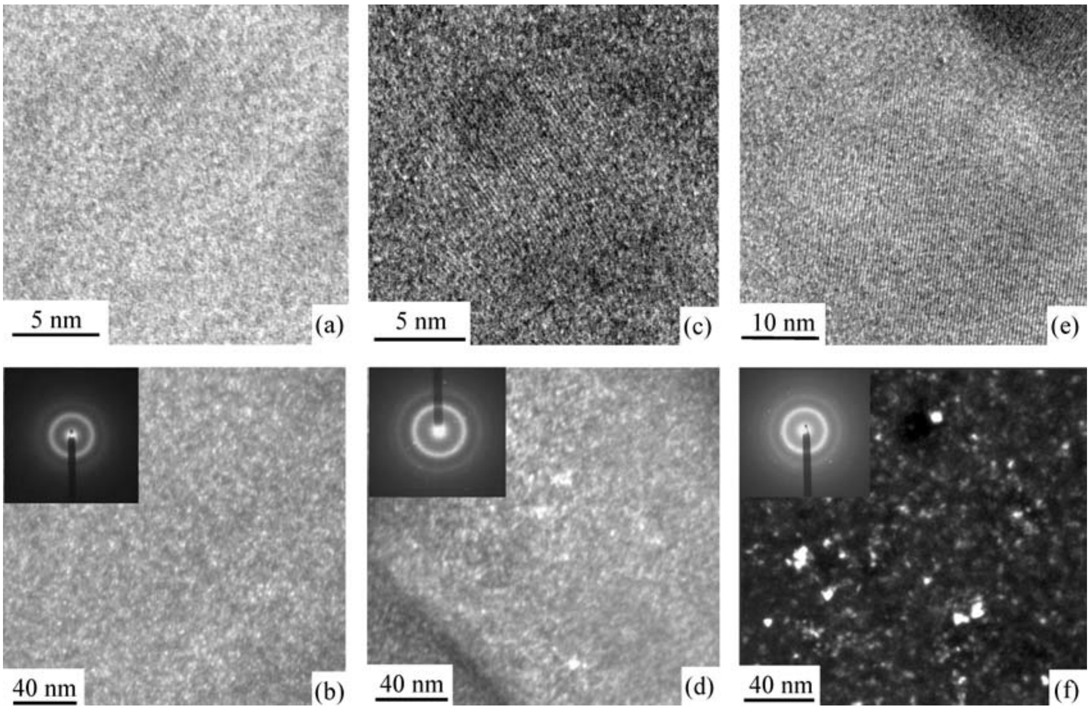

Figure 3 High resolution image (a) and dark field image with SAED pattern (b) of the specimen annealed at 676 K for 360 s; high resolution image (c) and dark field image with SAED pattern (d) of the specimen annealed for 600 s; high resolution image (e) and dark field image with SAED pattern (f) of the specimen annealed for 1200 s.

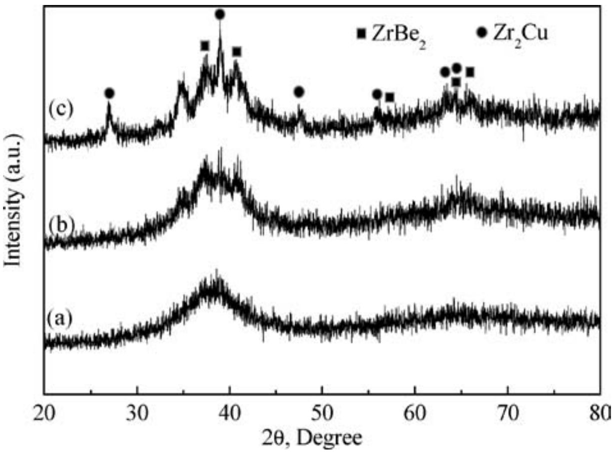

Figure 4 XRD patterns of the BMG annealed for different times at 676 K. (a) 360 s; (b) 600 s; (c) 1800 s.

Fig. 3e and f). It is obvious that, in this case, the nanocrystal distribution is inhomogeneous and the average size of the nanocrystals increases to approximately 30 nm.

Fig. 4 shows the XRD patterns obtained from the specimens annealed at 676 K for 360, 600 and 1200 s. It can be seen that the amount of the nanocrystalline phases in the BMG annealed for 360 s is not high enough to yield any reflection in XRD pattern (see Fig. 4a). During the annealing period from 600 to 1200 s, some Bragg peaks appear in the XRD patterns (see Figs 4b and c). The calculation of d-spacings obtained from the sharp peaks points to two main phases: a $ZrBe_2$ hexagonal phase ($a = 3.820$ Å, $c = 3.239$ Å) and a Zr_2Cu tetragonal phase ($a = 3.220$ Å and $c = 11.183$ Å). These phases are similar to those reported in Ref. [22].

3.2. Mechanical properties

The as-quenched BMG and the BMGs annealed at 676 K for different times, i.e. 180, 360, 600 and 1200 s, are tensile tested at room temperature. All specimens exhibit a perfect elastic deformation without yielding and plastic deformation before fracture. The corresponding tensile fracture strength and elastic modulus are listed in Table I. The tensile tests show that the fracture strength does not change obviously for the BMG annealed for 180 s, i.e. upon structural relaxing, as compared to that of the as-quenched BMG. However, for BMGs with a duplex phase structure consisting of nanocrystalline phase and amorphous phase, the fracture strength decreases with the increase in the crystallized volume fraction and in the size of the nanocrystalline phase, whilst the Young's modulus gradually increases with annealing time prolonged. These data suggest that precipitation and growth of the nanocrystalline phases in the annealing process induce significant embrittlement of the BMG.

Micro hardness (Hv) test indicates that the value of Hv increases with annealing time prolonged (see Table I). The measurements of hardness were carried out with different loads, i.e. 25, 100, 300, 500 and 1000 g. At each load, the indentation is repeated five times to avoid the occasional change in hardness. All Hv values are mean values measured at five loads. It is evident that a hardening phenomenon occurred as the BMG is annealed in the supercooled liquid region.

3.3. SEM observations

The fracture surface morphologies for tensile deformation of as-quenched BMG and BMG annealed for 180 s are shown in Fig. 5. It can be seen that the fracture features for these two specimens are almost same. Both fracture angles, which are an angle between tensile axis and the fracture plane, are measured to be 56° (see Fig. 5a and c). Typical feature of BMGs under room-temperature tensile deformation, i.e. vein-like pattern with round cores and liquid droplets, are observed on the entire fracture surface (see Fig. 5b and d). The round core structure is considered as an origination of local

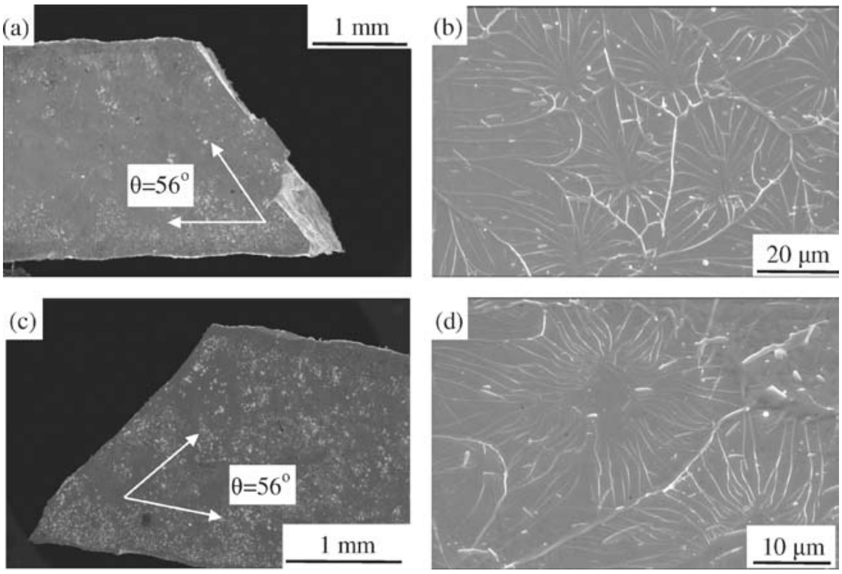

Figure 5 SEM images showing the tensile fracture surfaces of the as-quenched and annealed BMGs. (a) Side view and (b) top view of the as-quenched BMG; (c) side view and (d) top view of the BMG annealed for 180 s.

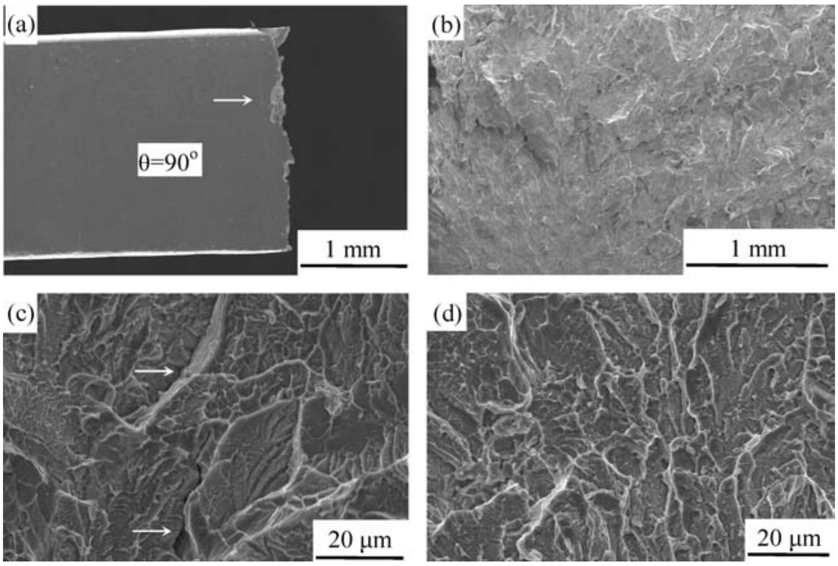

Figure 6 SEM images showing the tensile fracture surface of the BMG annealed for 360 s. (a) Side view; (b) top view; (c) step-like structure and microcracks; (d) vein-like pattern and liquid droplets.

shear band and "pulled out" by normal stress [23]. Once the round core forms, the viscosity of the amorphous phase in the shear band decreases due to the increase in quantity of free volume [24] and then a viscous layer is generated on the fracture surface. Under the shear stress, as a driving force, the viscous layer propagates outwards from the centre of the round core, which produces the vein-like pattern. As the vein-like patterns originating from different round cores encounter each other, the ridgelines are formed. The specimen should be ultimately torn off from the ridgelines. These features display that the deformation behaviours of specimens as-quenched and annealed for 180 s exhibit a shear fracture mechanism that is dominated by the formation and propagation of localized shear bands on the fracture surface [21, 25–27]. Although the specific heat measurement suggests that the free volume is reduced in quantity for the BMG annealed for 180 s, the fracture behaviour does not evidently differ, respect to the fracture behavior of the as-quenched BMG. The appearance of the liquid droplets on the fracture surface indicates occurrence of the adiabatic heating [27].

Fig 6 shows the fractography of the BMG annealed for 360 s. The fracture angle increases to be 90° as shown in Fig. 6a. The morphology of the fracture surface shows much difference from that of the as-quenched BMG. The round core pattern is invisible. The fracture surface is uneven on micro area, as shown in Fig. 6b. At higher magnification, vein-like pattern plus step-like structure and some liquid droplets are clearly seen in Fig. 6c and d. Each step-like pattern is attached by a crack, as marked by arrows in Fig. 6c. As compared to the as-quenched BMG, the presence of crack is an important characteristic appearing on the fracture surface and the specimen surface. Considering the presence of nanocrystals on the amorphous phase matrix after annealing for 360 s, the nanocrystallization is a possible reason resulting in the formation of cracks. Once the crack is formed under the tensile stress, it propagates rapidly and fracture occurs. Subsequently, the propagation of the crack generates the uneven fracture surface and the step-like structure. The presence of the vein-like pattern suggests that the viscous layer is also formed on the fracture surface. Since the crystallized volume fraction is only 13%, the local shear band should be "pulled out" by normal stress in the residual amorphous phase. The viscous layer is also generated within the shear band. However, due to the fracture angle of 90°, the shear stress is absent. The round core pattern can not be formed without the shear stress driving. In addition, the adiabatic heating phenomenon also occurs due to large amount of residual amorphous phase.

The fractography of the BMG annealed for 600 s is shown in Fig. 7. The fracture angle is also 90° (see Fig. 7a). Some cracks appear on the fracture surface, as shown in Fig. 7b. Further enlarging one of cracks, river pattern is observed (see Fig. 7c) and these river patterns originate from some microcracks as marked by arrows in Fig. 7c. As two neighbour river patterns encounter, the crack is formed (see Fig. 7c). With the crack proceeding, the fracture surface is torn off layer by layer, as shown in Fig. 7d. The tearing off generates cracks on the specimen's surface, as shown by an arrow in Fig. 7a. The liquid droplets and vein-like pattern are also observed on the fracture surface (see Fig. 7e), representing the adiabatic heating also happening and the formation of the viscous layer on the amorphous phase matrix, which are similar to those in the BMG annealed for 360 s. Based on these observations, it is obvious that the fracture also results from the formation and propagation of cracks. Furthermore, the formation of cracks and the fracture surface being torn off layer by layer imply that the brittlement of the BMG is deteriorated due to the increment in the crystallized volume fraction (29%) and the size (15 nm) of the nanocrystalline phase.

Fig. 8 shows the fractography of the BMG annealed for 1200 s. From the side view of the fracture surface (see Fig. 8a), it is seen that the fracture surface is not very flat. Mirror region (region A) and stripping-off region (region B) occupy the entire fracture surface

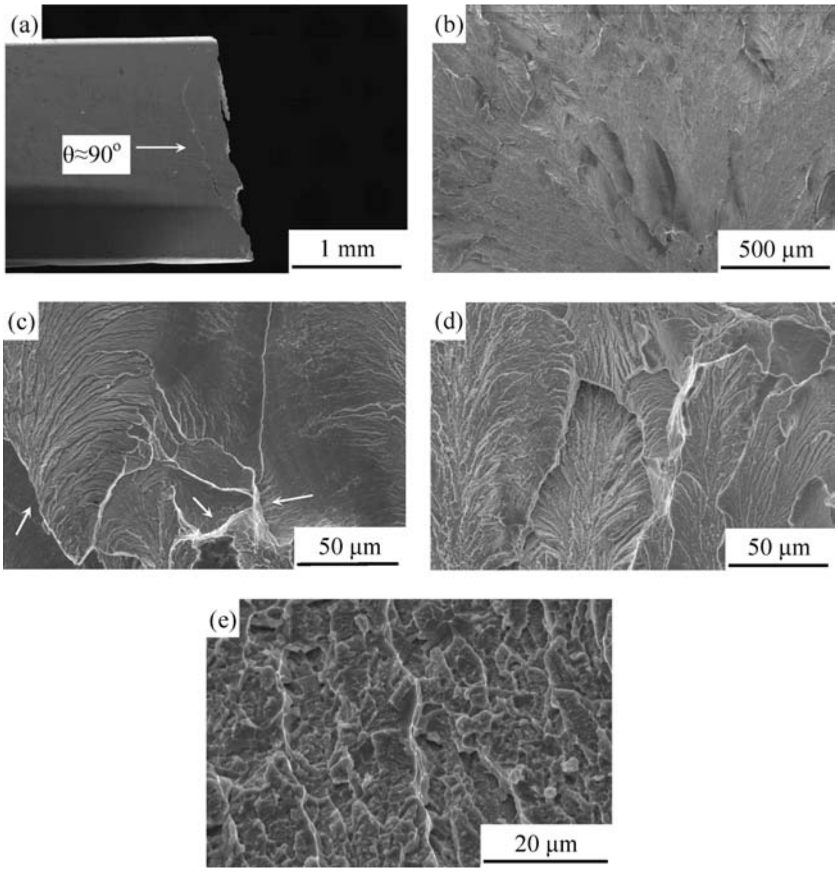

Figure 7 SEM images showing the tensile fracture surface of the BMG annealed for 600 s. (a) Side view; (b) top view; (c) macrocrack and river patterns [micromorphology corresponding to region A in (b)]; (d) fracture surface torn off layer by layer; (e) vein-like pattern and liquid droplets.

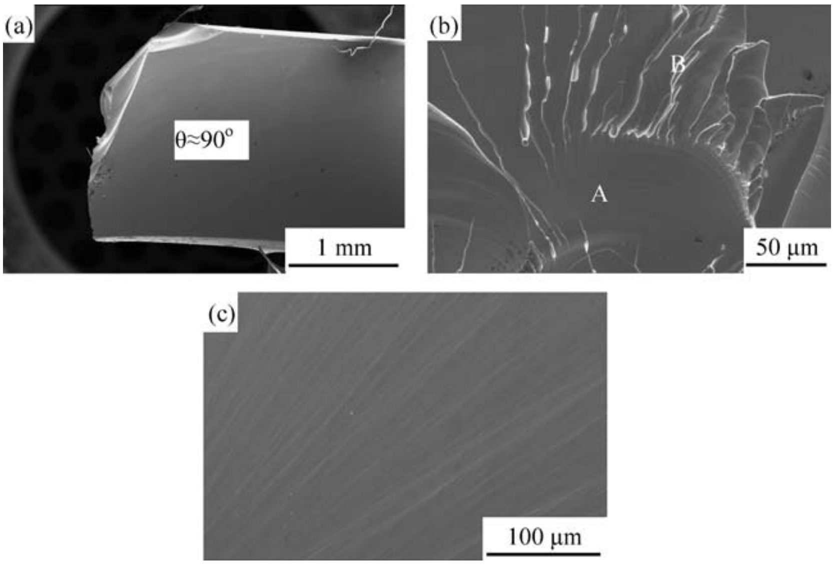

Figure 8 SEM images showing the tensile fracture surface of the BMG annealed for 1200 s. (a) Side view; (b) mirror region and tearing-off region; (c) detail of the mirror region.

(see Fig. 8b). Fig. 8c shows the mirror region at large magnifications, which exhibits some faint fracture slip lines. The formation of mirror region suggests that the fracture in this region is a fast fracture process [28]. The fast fracture needs the matter containing plenty of cracks on the fracture surface because the fracture fast advance usually depends on cracks joining together to form continuous crack propagation. During the terminal stage of fast fracture, the crack front outspaces the crack matter, with continued crack extension taking place through boundless of secondary cracks that form at the crack tip, which generates the stripping-off region attaching on the mirror region. The vein-like pattern and the liquid droplets appearing on the fracture surface of the BMG annealed for shorter time (less than 600 s) can not be observed for the BMG annealed for 1200 s.

Indents produced by micro indentation are also observed by SEM. Fig. 9 shows the features of indents which are indented under a load of 100 g. A circular

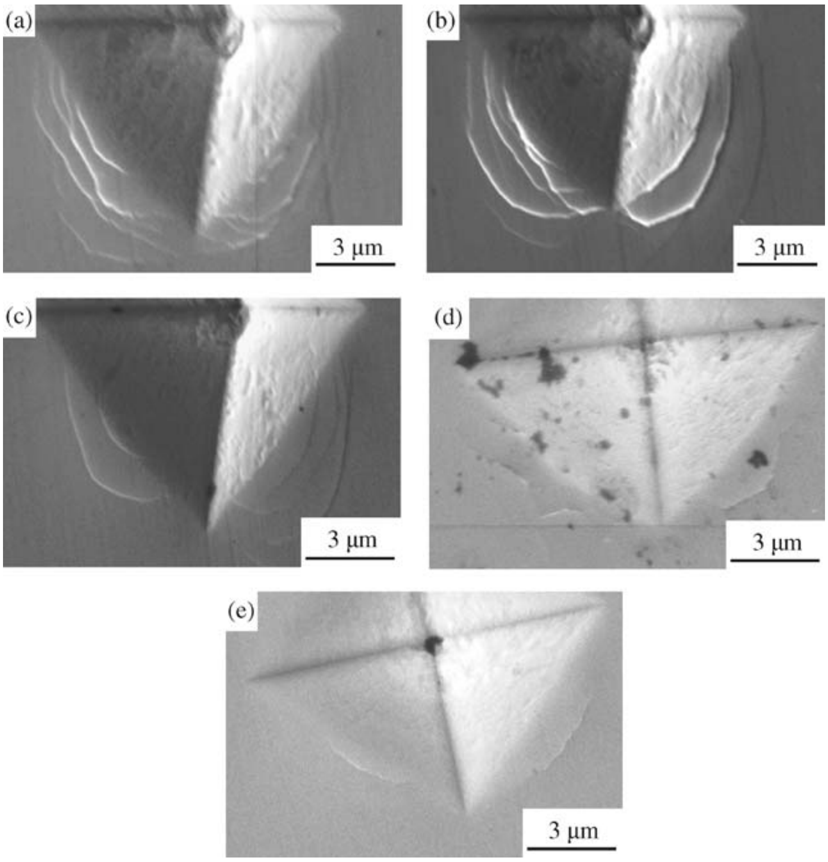

Figure 9 SEM images showing the indents for BMGs annealed for different times under the load of 100 g. (a) As-quenched; (b) 180 s; (c) 360 s; (d) 600 s; (e) 1200 s.

deformation region characterizes indent morphologies of specimens as-quenched and annealed for 180 s as shown in Fig. 9a and b, which represents overlapping layers of displace material. According to Ref. [29], this circular pattern is generated by serrated flow behavior that occurs under the compressive load. The serrated flow is a discrete burst of individual shear band around the indent. Therefore, the circular pattern can be considered as a pile-up of shear bands. For the BMG annealed for 360 s, the quantity of circular patterns decreases with the hardness increasing, as shown in Fig. 9c. In the case of annealing for 600 and 1200 s, much less circular patterns are observed around indents (see Fig. 9d and e). It is, therefore, demonstrated that the discrete serrated plastic deformation transforms to a continuous plastic deformation with the annealing time prolonged.

4. Discussion

Based on the fractographic observations, we find three kinds of fracture behaviours with crystallized volume fraction increasing, i.e. the shear fracture, the crack induced fracture and the fast fracture.

The deformations of the as-quenched and structural relaxed (annealed for 180 s at 676 K) BMGs are covered in the shear fracture. In this case, the structure of material is fully amorphous. The reduction in the free volume due to the structural relaxation leads to the amorphous phase being densified that results in the increment in the Young's modulus and the hardness. However, although elastic deformation ability of the structural relaxed BMG decreases due to the increase in the Young's modulus, the fracture behaviour is not influenced. The forming and propagation of localized shear bands is the main deformation mechanism dominating the fracture behaviour (cf. Fig. 5d). Shear bands formed under the indent further confirm that the shear band formation would not be affected by the structural relaxation (cf. Fig. 9b).

The nanocrytalline phase embedding in the amorphous matrix do significantly influence the deformation. The fracture surface observations indicate that the BMG with the nanocrystalline phase small in size (5–15 nm) and crystallized volume fraction (13–29%) exhibits the crack resulting in fracture. The shear band can not be observed but the microcrack appears on the fracture surface and specimen surface (cf. Figs 6a, c and 7a, c). The increase in Young's modulus and decrease in the tensile fracture strength suggest that nanocrystalline phase and amorphous phase coexisting structure is more brittle than the monolithic amorphous phase structure. There are two possible reasons for the nanocrystallization induced embrittlement of the BMG. One reason is a stress concentration near the interface between the amorphous phase and the crystalline phase [16]. The stress concentration will increase as the size of crystalline phase increases [30]. As the size and volume fraction of the nanocrytalline phase increase, more cracks should be generated due to tensile stress. Once cracks appear on the phase interface, the unstable expanding of the cracks is another reason influencing the fracture. According to the Griffith crack theory [13, 28], the increment in the elastic modulus will reduce the plastic deformation ability in the crack tip zone. Referring the tensile test results in Table I, the Young's modulus increases with the annealing time prolonged, which makes the crack propagating more easily. In Refs. [9–12, 21], authors have reported that the presence of nanocrystalline phase with small size and volume fraction would enhance the fracture strength. The strengthening mechanism was usually attributed to the presence of nanocrystal suppressing the shear band forming and propagating. However, in our present work, for the $Zr_{41.25}Ti_{13.75}Ni_{10}Cu_{12.5}Be_{22.5}$ BMG, the primary crystallization and the main crystallization at the initial stage produce nanocrystalline phase with size of from 5 to 15 nm and the volume fraction of from 13 to 29%, which promote the crack forming in the BMG. In addition, due to the elastic deformation ability decreasing, the crack propagation in the annealed BMG is easier than that in monolithic amorphous phase.

The fast fracture occurs in the BMG annealed for a longer time (1200 s). In this case, the nanocrystalline phase further grows to 30 nm and its volume fraction reaches 53%. Large amounts of nanocrytals should bring out the formation of high-density microcracks in the BMG as the tensile stress is applied. Under the tensile stress, the cracks propagate and join together to form continuous cracks, and finally the fast fracture happens at a lower tensile stress.

Although the nanocrystallization results in embrittlement of the BMG, the micro hardness test indicates a strengthening phenomenon under the indentor tip. The deformation behaviour of the BMG under the indentor tip gradually changes from the discrete serrated plastic deformation to the continuous plastic deformation, implying that the formation of shear band is suppressed due to the evolution of nanocrystalline phase. The effect of the nano-scale particles on the shear band formation is twofold. One case is that the size of the nanocrystal is smaller than the thickness of shear band. In this case, nanocrystal appears within shear band, which will improve the viscosity of the amorphous phase in shear band. As a result, the shear band operating needs higher pressure and then hardness is improved. In contrast, the presence of the nanocrystals larger than the thickness of shear band may obstruct the formation and propagation of an individual shear band. In order to accommodate the pressure load, more shear bands would be required at every instant and then the hardness is also improved. Because these shear bands are obstructed in a fine length scale by nanocrystalline phase, the indent morphology shows the continuos deformation characteristic [10, 29, 31]. Therefore, the nanocrystalline phase, whether the size is lager or smaller than the thickness of shear band, should influence the deformation behaviour at the indentor tip. In the present study, although the shear band thickness is still not known, the nanocrystalline phase evolution influencing the deformation behaviour at the indentor tip is observed. The as-quenched and structural relaxed BMGs exhibit the formation and propagation of the shear band upon the indentation pressure applied. The circular pattern characterises the pile-up of shear bands (cf. Fig. 9a and b). In the primarily crystallized BMG with small nanocrystals (size of 5 nm and volume fraction of 13%), the shear band operating is more difficult than that in the as-quenched BMG, which leads to the reduction in the quantity of the shear band and increase in hardness (cf. Fig. 9c). As the main crystallization occurs, with the size and the volume fraction of nanocrystalline phase reaching 30 nm and 53% respectively, the formation and propagation of the shear band are completely obstructed. The continuous to discrete serrated deformation transformation at the indentor tip is observed (cf. Fig. 9d and e).

5. Summary

In the present study, the effect of microstrutural evolution on mechanical properties of the $Zr_{41.25}Ti_{13.75}Ni_{10}Cu_{12.5}Be_{22.5}$ BMG isothermally annealed in the supercooled liquid region are studied by DSC, TEM, tensile deformation and micro hardness test. The following conclusions can be made:

1. As the BMG is annealed in the supercooled liquid region (676 K), the evolution process of the amorphous phase is divided along the annealing time into three stages. At first stage, structural relaxation annihilates the free volume pre-existing in the amorphous phase and the crystallization is not activated. At the second stage, primary crystallization occurs and produces the nanocrystalline phase with size of 5 nm and volume fraction of 13% embedding in the amorphous phase matrix. At third stage, main crystallization happens, which results in further growth of the nanocrystlline phase. The size and the volume fraction of the nanocrystalline phase reaches 30 nm and 53% respectively. The main crystallization produces can be identified to be $ZrBe_2$ and Zr_2Cu phases.
2. The fracture strength decreases and the Young's modulus increases with the nanocrystlline phase precipitating and growing. The structural relaxation due to isothermally annealing does not significantly influence the deformation behavior of the BMG. However, once the nancorystalline phase precipitates, the formation and propagation of cracks rather than shear bands dominate the fracture behavior, which results in the reduction of the fracture strength.
3. The presence of nanocrystals can obstruct the formation of the shear band at the indenter tip and enhance the viscosity of the amorphous phase in the shear band, which is the main strengthening mechanism under the indentation pressure.

Acknowledgements

This work is partly supported by Harbin Institute of Technology Foundation. The assistance of staff and use of TEM in the Electron Microscopy Unit at ANU is acknowledged.

References

1. W. L. JOHNSON, *MRS Bull.* **24**(10) (1999) 42.
2. Z. P. LU and C. T. LIU, *Acta Mater.* **50** (2002) 3501.

3. Y. KAWAMURA, T. SHIBATA, A. INOUE and T. MASUMOTO. *ibid.* **46**(1) (1998) 253.
4. Y. SAOTOME, T. HATORI, T. ZHANG and A. INOUE, *Mater. Sci. Eng. A* **304–306** (2001) 716.
5. J. SHEN, G. WANG, J. F. SUN, Z. H. STACHURSKI, C. YAN, L. YE and B. D. ZHOU, *Intermetallics* **13** (2005) 79.
6. T. G. NIEH, J. WADSWORTH, C. T. LIU, T. OHKUBO and Y. HIROTSU, *Acta Mater.* **49** (2001) 2887.
7. W. J. KIM, D. S. M. A and H. G. JEONG, *Scr. Mater.* **49** (2003) 1667.
8. D. H. BAE, H. K. LIM, S. H. KIM, D. H. KIM and W. T. KIM, *Acta Mater.* **50** (2002) 1749.
9. L. Q. XING, D. M. HERLACH, M. CORNET, C. BERTRAND, J.-P. DALLAS, M.-F. TRICHET and J.-P. CHEVALIER, *Mater. Sci. Eng. A* 226–228 (1997) 874.
10. A. INOUE, C. FAN, J. SAIDA and T. ZHANG, *Sci. Tech. Adv. Mater.* **1** (2000) 73.
11. T. K. HAN, T. ZHANG, A. INOUE, Y. S. YANG, I. B. KIM and Y. H. KIM, *Mater. Sci. Eng. A* **304–306** (2001) 892.
12. J. ECKERT, M. SEIDEL, L. Q. XING, I. BÖRNER and B. WEIB, *Nanostructured Mater.* **12** (1999) 439.
13. M. YAN, J. F. SUN and J. SHEN, *J. Alloys Comp.* **381**(1/2) (2004) 86.
14. U. RAMAMURTY, M. L. LEE, J. BASU and Y. LI, *Scr. Mater.* **47** (2002) 107.
15. N. NAGENDRA, U. RAMAMURTY, T. T. GOH and Y. LI, *Acta Mater.* **48** (2000) 2603.
16. Z. BIAN, G. L. CHEN, G. HE and X. D. HUI, *Mater. Sci. Eng. A* **361** (2001) 135.
17. A. PEKER and W. L. JOHNSON, *Appl. Phys. Lett.* **63**(17) (1993) 2342.
18. S. SCHNEIDER, P. THIYAGARAJAN and W. L. JOHNSON, *ibid.* **68**(4) (1996) 493.
19. B. P. KANUNGO, S. C. GLADE, P. ASOKA-KUMAR and K. M. FLORES, *Intermetallics* **12** (2004) 1073.
20. A. VAN DEN BEUKEL and J. SIETSMA, *Acta Mater.* **38** (1990) 383.
21. Z. BIAN, G. HE and G. L. CHEN. *Scr. Mater.* **46** (2002) 407.
22. I. MARTIN, T. OHKUBO, M. OHNUMA, B. DECONIHOUT and K. HONO, *Acta Mater.* **52**(15) (2004) 4427.
23. X. S. XIAO, S. S. FANG, L. XIA, W. H. LI, Q. HUA and Y. D. DONG, *J. Non-cryst. Solids* **330** (2003) 242.
24. F. SPAEPEN, *Acta Metall.* **25** (1977) 407.
25. G. HE, J. LU, Z. BIAN, D. J. CHEN, G. L. CHEN, G. C. TU and G. J. CHEN, *Mater. Trans. JIM* **42**(2) (2001) 356.
26. Z. F. ZHANG, G. HE, J. ECKERT and L. SCHULTZ, *Phys. Rev. Lett.* **91**(4) (2003) 045505.
27. C. T. LIU, L. HEATHERLY, D. S. EASTON, C. A. CARMICHAEL, J. H. SCHNEIBEL, C. H. CHEN, J. L. WRIGHT, M. H. YOO, J. A. HORTON and A. INOUE, *Matell. Mater. Trans.* **A29** (1998) 1811.
28. R. W. HERTZBERG, in "Deformation and Fracture Mechanics of Engineering Materials" 4th edition (John Wukey & Sons, INC., Brisbane, 1996) p. 299.
29. B. C. WEI, T. H. ZHANG, W. H. LI, Y. F. SUN, Y. YU and Y. R. WANG, *Intermetallics* **12** (2004) 1239.
30. J. GURLAND and J. PLATEAU, *Trans. ASM* **56** (1963) 442.
31. A. L. GREER and I. T. WALK, *Mater. Sci. Forum* **386–388** (2002) 77.

Received 29 December 2004
and accepted 25 March 2005